Heavy-Ion Physics at the LHC with ALICE

Raimond Snellings for the ALICE collaboration
NIKHEF, Kruislaan 409, 1098 SJ Amsterdam, The Netherlands

In addition to proton-proton collisions at 14 TeV center of mass energy the LHC will provide lead on lead collisions at an energy of 5.5 TeV per nucleon. ALICE is a general-purpose heavy-ion experiment designed to study the physics of strongly interacting matter and the quark-gluon plasma in nucleus-nucleus collisions at the LHC. In these lectures we present a brief overview of the most important results obtained at RHIC and the SPS and discuss the prospects of heavy-ion physics with ALICE at the LHC. More details about the recent discoveries made at RHIC can be found in the lecture notes of J. Nagle [1].

1. THE QCD PHASE TRANSITION AND EQUATION OF STATE

In the last thirty years particle physics has led to a profound understanding of the world around us, summarized in the so-called "Standard Model". It provides a coherent and precise description of the building blocks of matter and the three fundamental interactions: the weak, the strong and the electromagnetic. However, at the same time we realize that this model is far from complete. In fact we have learned that we do *not* know what most of the universe is made of. To answer the questions, what the universe is made of and how it works, is the ultimate challenge of particle physics [2, 3].

In our current understanding, the universe went through a series of phase transitions after the Big Bang. These phase transitions mark the most important epochs of the expanding universe. At 10^{-11} s after the Big Bang and at a temperature $T \sim 100$ GeV ($\sim 10^{15}$ K) the electroweak phase transition took place. At this time most of the known elementary particles acquired their Higgs masses [4–6]. At 10^{-5} s and at a temperature three orders of magnitude lower (170 MeV $\sim 10^{12}$ K), the strong phase transition took place. During the strong phase transition the quarks and gluons became confined in hadrons. At the same time the approximate chiral symmetry was spontaneously broken. This symmetry is crucial in the standard model and gives rise to the presence of the light pions [7].

The underlying theory of the strong force, QCD, is well established even though its fundamental degrees of freedom, the quarks and gluons, cannot be observed as free particles due to confinement. The known QCD Lagrangian provides in principle the complete picture but the QCD field equations are notoriously hard to solve. In fact, the two most important and interesting properties, confinement and chiral symmetry breaking, are still poorly understood from first principles.

One of the key features of QCD is that the strength of the coupling between quarks and gluons depends on their relative momenta. At higher momenta and thus smaller distances the coupling becomes weaker, leading to so called asymptotic freedom [8, 9]. Therefore, in a QCD system at very high temperatures the quarks and gluons are expected to become quasi-free so that the bulk properties can be described by an ideal gas Equation of State (EoS). This deconfined dense state of matter is called a Quark Gluon Plasma (QGP). Properties like energy density and pressure provide direct information about the EoS and thus about the basic degrees of freedom.

Dimensional arguments allow us to estimate the critical energy density $\epsilon_c \sim 1$ GeV/fm^3 and temperature $T_c \sim 170$ MeV. However these values imply that the transition occurs in a regime where the coupling constant is of order unity, casting doubts on results of perturbative calculations. Better understanding of the non-perturbative domain comes from lattice QCD calculations, where the field equations are solved numerically on a discrete space-time grid. Lattice QCD provides quantitative information on the QCD phase transition between confined and deconfined matter and the EoS. Figure 1a shows the calculated energy density as a function of temperature [10]. It is seen that the energy density changes rapidly at the critical temperature $T_c \sim 170$ MeV, which is due to the rapid increase in the effective degrees of freedom. From these lattice calculations it follows that at T_c not only deconfinement sets in but that also chiral symmetry is restored. The pressure, shown in Fig. 1b, changes slowly at T_c compared to the rapid increase of the energy density. Therefore the pressure gradient in the system, $\mathrm{d}P/\mathrm{d}\epsilon$, is significantly reduced during the phase

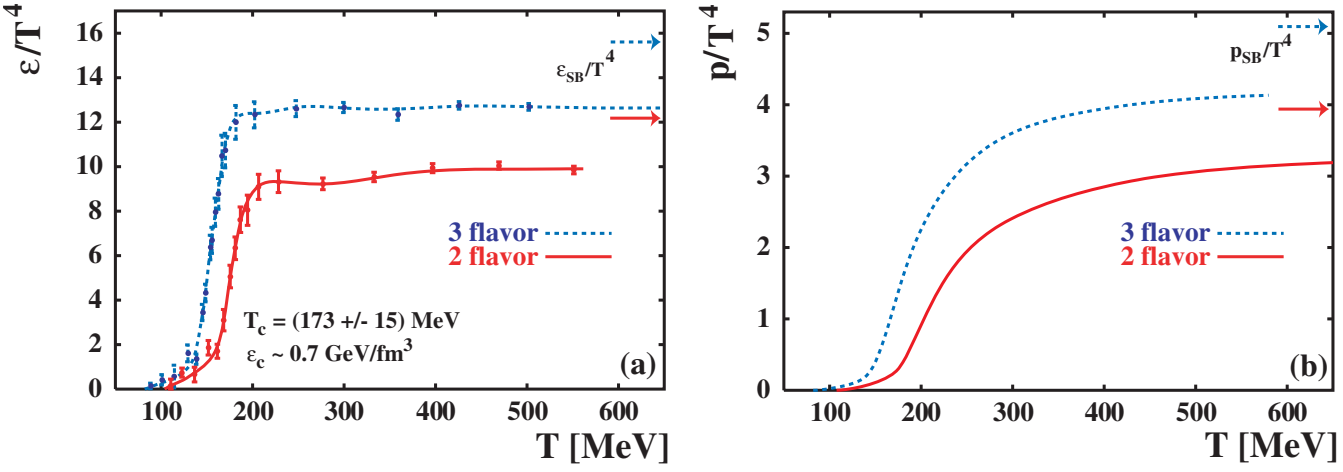

Figure 1: a) Energy density ϵ as a function of temperature from lattice calculations [10]. For an ideal gas the energy density is proportional to the number of thermal degrees of freedom. This causes the sharp increase at T_c where the system goes from a pion gas, $g = 3$, to a quark gluon plasma where $g = 37$ in case of two quark flavors. The arrows in the figure indicate the ideal Stefan-Boltzmann values. b) The pressure from lattice calculations versus the temperature. The pressure also reflects the number of degrees of freedom but changes slowly at the phase boundary.

transition.

In the limit of an ideal Stefan-Boltzmann gas the EoS of a QGP is given by:

$$P_{\rm SB} = \frac{1}{3}\epsilon_{\rm SB}, \quad \epsilon_{\rm SB} = g\frac{\pi^2}{30}T^4, \tag{1}$$

$$g = n_f \times 2_s \times 2_q \times 3_c \times \frac{7}{8} + 2_s \times 8_c, \tag{2}$$

where $P_{\rm SB}$ is the pressure, $\epsilon_{\rm SB}$ the energy density and T the temperature. Each bosonic degree of freedom contributes $\frac{\pi^2}{30}T^4$ to the energy density; each fermionic degree of freedom contributes $\frac{7}{8}$ of this value. The value of g is obtained from the sum of the appropriate number of flavors $\times$ spin $\times$ quark/antiquark $\times$ color factors for the quarks and spin $\times$ color for the gluons. The energy density for a two (three) flavor QGP, where $g = 37$ ($g = 47.5$) is an order of magnitude larger than for an hadron gas where $g \sim 3$. The corresponding Stefan-Boltzmann values of the energy density and pressure are plotted in Fig. 1a and Fig. 1b and show that the lattice results reach a significant fraction (0.8) of these values. The deviation from the Stefan-Boltzmann limit shows that the QCD system around T_c does *not* behave like a weakly interacting parton gas.

2. HEAVY-ION COLLISIONS

Figure 2a shows a theoretical phase diagram of nuclear matter for two massless quarks as function of temperature and baryon chemical potential. Relativistic heavy-ion collisions are a unique tool to test this phase diagram by studying deconfinement and the EoS of hot QCD matter under controlled conditions [11–16]. Like the early universe, the hot and dense system created in a heavy-ion collision will expand and cool down. In this time evolution the system probes a range of energy densities and temperatures, and possibly different phases. The evolution of the created system can be divided in two characteristic periods, see Fig. 2b. During the formation of the system ($\leq 3\times10^{-24}$ sec) collisions with large momentum transfer occur. During this period the largest energy density is created. The system will thermalize and form the QGP provided that the quarks and gluons undergo multiple interactions. Due to the thermal pressure, the system undergoes a collective expansion and eventually becomes so dilute that it hadronizes. In the hadronic phase it further cools down via inelastic and elastic interactions until it becomes non-interacting (the freeze-out stage).

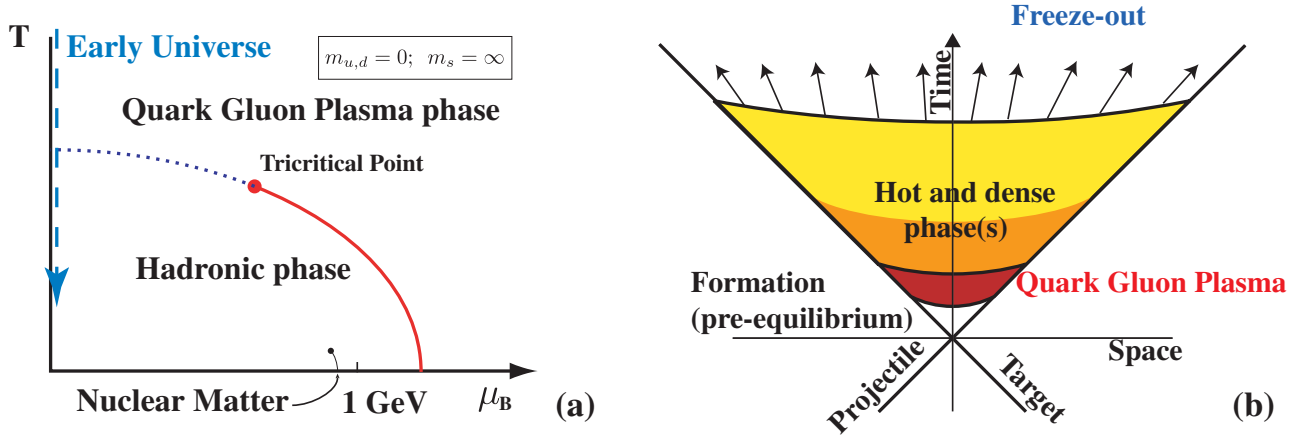

Figure 2: a) Theoretical phase diagram of nuclear matter for two massless quarks as function of temperature T and baryon chemical potential μ_B. b) Illustration of the characteristic periods in time for a heavy-ion collision.

To study QCD at extreme densities ultra relativistic heavy-ion experiments have been performed at the Brookhaven Alternating Gradient Synchrotron (AGS), the CERN Super Proton Synchrotron (SPS) and the Brookhaven Relativistic Heavy Ion Collider (RHIC) with maximum center of mass energies of $\sqrt{s_{\rm NN}} = 4.75$, 17.2 and 200 GeV respectively. The future Large Hadron Collider (LHC) will make Pb-Pb collisions available at an unprecedented energy of $\sqrt{s_{\rm NN}}$ = 5.5 TeV. Some of the main probes available in heavy-ion collisions will be described in the next section, together with some results which are considered to be the highlights of the experimental program so far.

2.1. Probes and observables

2.1.1. Event Characterization

Heavy ions are extended objects and the system created in a head-on collision is different from that in a peripheral collision. Therefore, collisions are categorized by their centrality. Theoretically the centrality is characterized by the impact parameter **b** which is, however, not a direct observable. Experimentally, the collision centrality can be inferred from the measured particle multiplicities if one assumes that this multiplicity is a monotonic function of **b**. Another way to determine the event centrality is to measure the energy carried by the spectator nucleons (which do not participate in the reaction) with Zero Degree Calorimetry (ZDC). A large (small) signal in the ZDC thus indicates a peripheral (central) collision.

Instead of by impact parameter, the centrality is often characterized by the so-called number of wounded nucleons or by the number of equivalent binary collisions. These measures can be related to the impact parameter **b** using a realistic description of the nuclear geometry in a Glauber calculation, see Fig. 3. Phenomenologically it is found that soft particle production scales with the number of participating nucleons whereas hard processes scale with the number of binary collisions.

2.1.2. Global observables

Examples of global observables which provide important information about the created system are the particle multiplicity and the transverse energy. Figure 4 shows the transverse energy versus the collision centrality as measured at $\sqrt{s_{NN}} = 130$ GeV by the PHENIX collaboration [17]. This measurement allows for an estimate of the energy density as proposed by Bjorken [18] for head-on collisions

$$\epsilon = \frac{1}{\pi R^2}\frac{1}{c\tau_0}\frac{{\rm d}E_{\rm t}}{{\rm d}y},$$

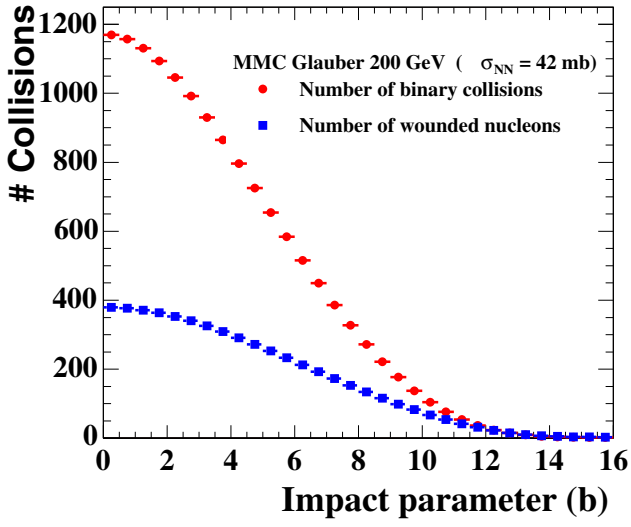

Figure 3: Number of wounded nucleons and binary collisions versus impact parameter.

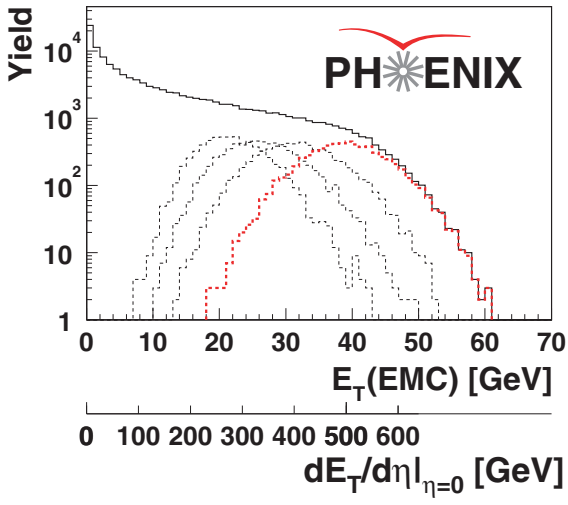

Figure 4: Transverse energy as a function of centrality as measured by PHENIX [17].

were R is the nuclear radius and τ_0 is the effective thermalization time (0.2-1.0 fm/c). From the measured $\langle dE_t/d\eta \rangle$ = 503 $\pm$ 2 GeV it follows that ϵ is about 5 GeV/fm^3 at RHIC. This is much larger than the critical energy density of 1 GeV/fm^3 obtained from Lattice QCD (see Fig. 1).

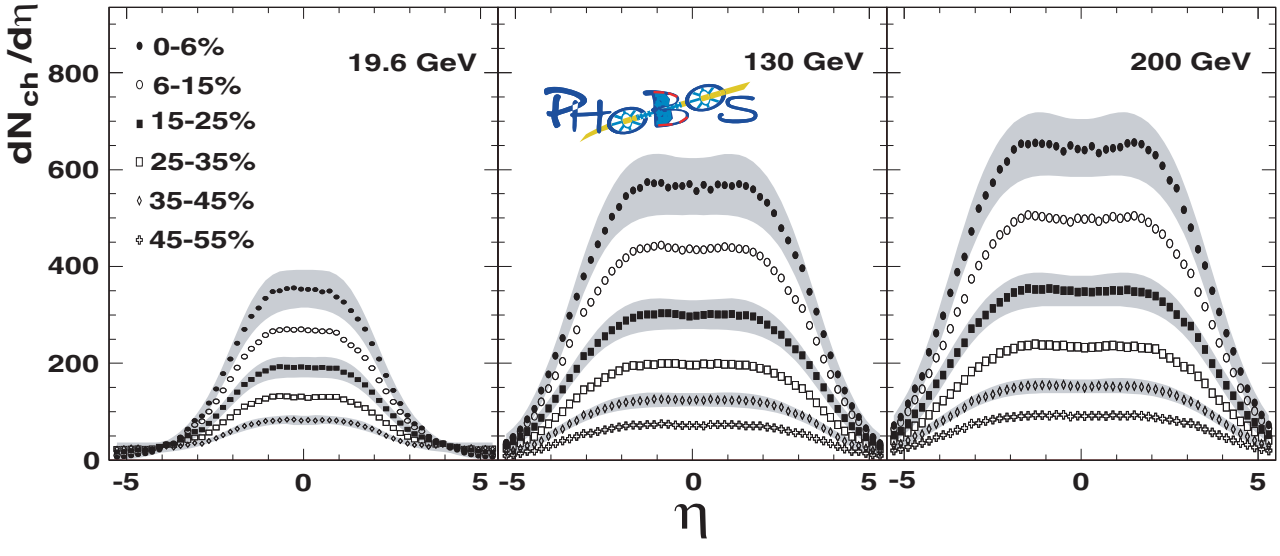

Figure 5: Multiplicity versus pseudo-rapidity for 19.6, 130 and 200 GeV measured by PHOBOS [19].

Figure 5 shows the charged particle multiplicity distributions versus the pseudorapidity η measured by PHOBOS at three different energies [19]. Notice that in total about 5000 charged particles are produced in the most central Au+Au collisions at the top RHIC energy.

2.1.3. J/Ψ suppression

One of the most promising QGP signatures at SPS energies has been the J/Ψ suppression predicted by T. Matsui and H. Satz [20]. This prediction is based on the idea that the confining potential in a QGP medium should screen the

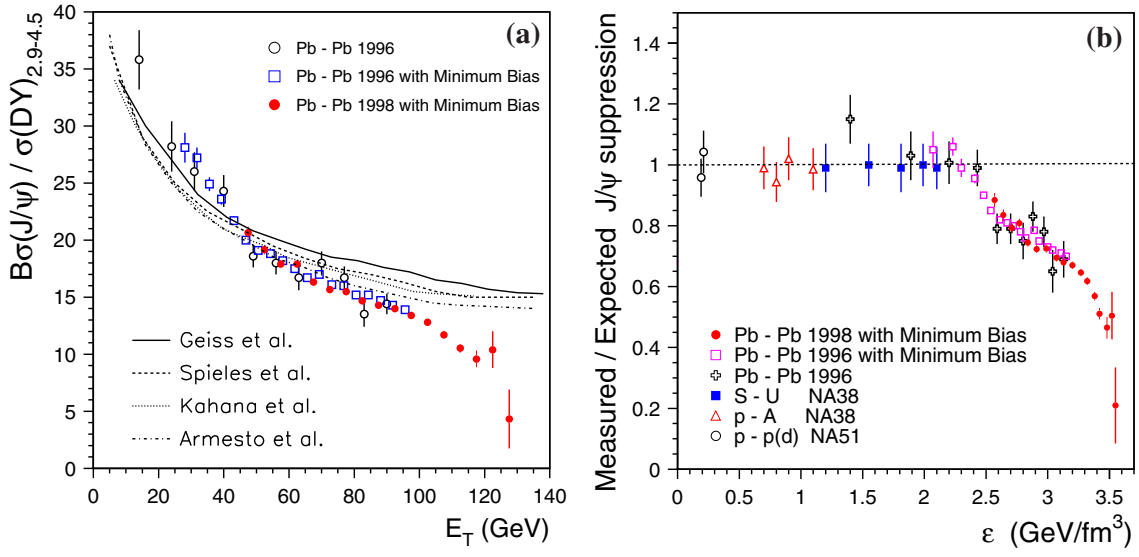

Figure 6: a) Comparisons between the NA50 Pb-Pb measured J/Ψ data and several conventional calculations of the suppression [21]. b) The J/Ψ anomalous suppression as a function of the energy density reached in the collisions. Suppression is obtained from the measured cross-sections divided by the values expected from nuclear absorption. For higher energy densities a abnormal suppression pattern is observed, as can be expected from charmonium melting due to deconfinement [21].

formation of a J/Ψ resonance from a $c\bar{c}$ pair. Results on the suppression obtained by the NA50 experiment are shown in Fig. 6. In Fig. 6a is shown the J/Ψ production normalized to the Drell-Yan yield, compared to calculations of the suppression expected in nuclear matter. In Fig. 6b is plotted the ratio of measured to expected J/Ψ suppression. For higher energy densities an anomalously large suppression is observed as is expected from charmonium melting in a QGP.

The PHENIX collaboration at RHIC also observed a significant J/Ψ suppression in central Au-Au collisions [22]. They have shown that the J/Ψ suppression at these higher energies is indeed larger than that expected from a extrapolating of cold nuclear matter effects as measured in d-Au collisions [23]. Contrary to expectations the suppression at RHIC is found to be as large as that at the SPS. The models that described the J/Ψ suppression at the SPS all predicted a significantly larger suppression at RHIC. At these RHIC energies however, central collisions produce multiple pairs of heavy quarks. These multiple c and $\bar{c}$ quarks, originally produced in separate incoherent interactions, might coalesce and form a J/Ψ [24]. This additional production mechanism complicates the interpretation, and can at RHIC be responsible for some regeneration of the J/Ψ yield.

2.1.4. Strangeness production

Strange particles produced in heavy-ion collisions give important information on the collision mechanism. In particular, if a phase transition to a QGP state takes place, one would expect an enhancement in the yields of strange and multi-strange particles in nucleus-nucleus reactions compared to those from proton-nucleus interactions [25–28]. In fact, the formation of such a state will lead to equilibration of strange quarks on a time scale of a few fm/c, and to the formation of multi-strange baryons and antibaryons close to thermal and chemical hadronic equilibrium. Their abundances will be frozen at the critical temperature T_c since hadronic reactions are too slow to compete with the rapid collective expansion of the fireball at temperatures below T_c. It is expected that the enhancement should be more pronounced for multi-strange than for singly strange particles. The experimental results on Λ, Ξ and Ω from the WA97/NA57 collaboration [29] are plotted in Fig. 7a and indeed show this predicted enhancement. However, the NA49 collaboration has found that this enhancement is already present in small colliding systems [30]. Since QGP formation in such small systems is perhaps less likely an other enhancement mechanism could be the reduction of canonical suppression in an extended system [31].

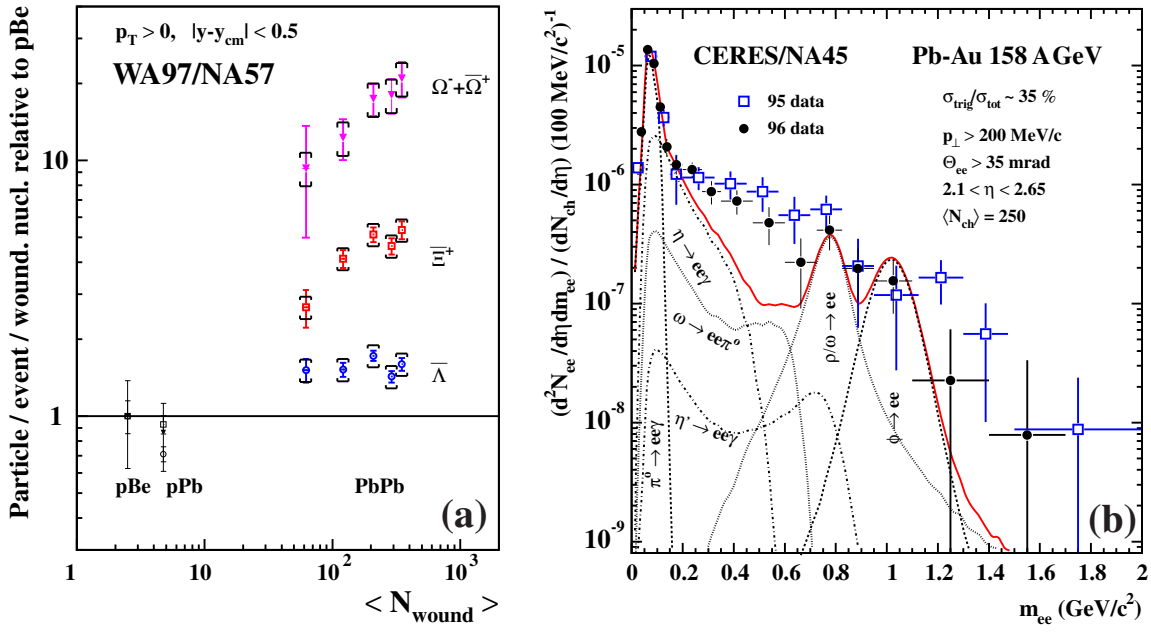

Figure 7: a) Strangeness enhancements measured by the NA57 experiment. The enhancements are defined as the particle yields normalized by the number of participating nucleons in the collision, and divided by the observed yield in proton-beryllium collisions. The yields expected from a simple superposition of nucleon-nucleon collisions would then lie on a straight line positioned at unity [29]. b) Normalized invariant-mass spectra of dilepton pairs. The measured yield is compared to the known hadronic decay sources, showing the individual contributions. At low invariant-mass a clear excess of the dilepton yield is observed

2.1.5. Dileptons

Correlated electron-positron pairs (dileptons) provide a probe of the expanding system at an early stage. The absence of any final state interaction conserves the primary information within the limits imposed by the space-time folding over the emission period. In the low-mass region, the thermal radiation is dominated by the decays of the light vector mesons ρ, ω, and ϕ. The ρ is of particular interest, due to its short lifetime of 1.3 fm/c, therefore its in-medium behavior around the critical temperature provides a direct link to chiral symmetry restoration. The shape of the measured dilepton yield by NA45/CERES, see Fig. 7b, can be explained by a strong medium modification of the intermediate ρ. This modification can theoretically be described by a reduction in mass (as a precursor of chiral symmetry restoration), known as Brown-Rho scaling [32, 33], or by a spreading of the width in a hadronic medium [34]. More recent experimental results from the NA60 collaboration, with much improved accuracy, show that the space-time averaged ρ spectral function is strongly broadened, but not shifted in mass [35].

2.1.6. Particle yields

The integrated yield of the various particle species provides information on the production mechanism and the subsequent inelastic collisions. A very successful description of the relative particle yields is given by the thermal model. In Fig. 8 the yield ratios measured at RHIC are compared to predictions from a thermal model fit [36]. The results from the fit show that all particles ratios are consistent with a thermal description using a single temperature and a single chemical potential. The resulting chemical freeze-out temperature of 176 MeV is very close to the critical temperature as calculated in lattice QCD (see Fig. 1a). Note, however, that a thermal description of particle yields in e^+e^- collisions gives a comparable temperature [37]. A recent discussion on statistical hadronization vs. chemical reaction dynamics can be found in [38].

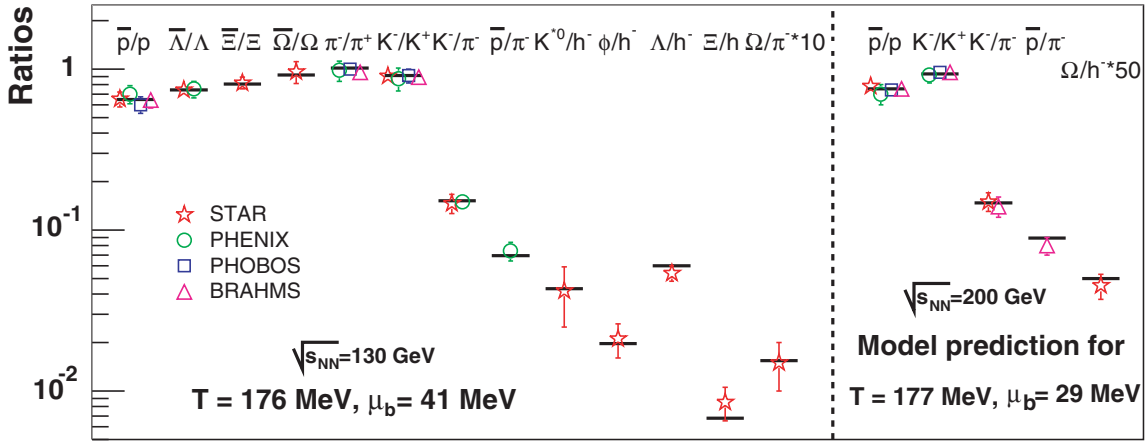

Figure 8: Particle yield ratios at RHIC compared with a thermal model [36].

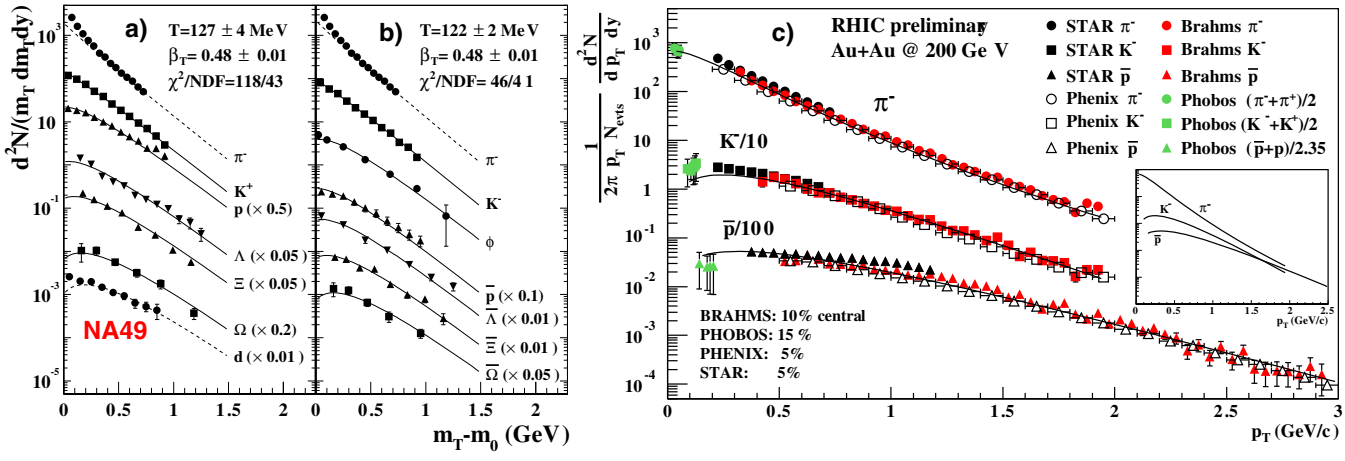

Figure 9: NA49 (SPS) and RHIC low-p_t spectra [39–44].

2.1.7. Spectra

The particle spectra provide much more information than the integrated particle yields alone. The particle yield as a function of transverse momentum reveal the dynamics of the collision, characterized by the temperature and transverse flow velocity of the system at kinetic freeze-out. As already mentioned above, kinetic freeze-out corresponds to the final stage of the collision when the system becomes so dilute that all interactions between the particles cease to exist so that the momentum distributions do not change anymore. Figure 9a and b show the transverse momentum distributions at $\sqrt{s_{\rm NN}} = 17$ GeV from NA49 [39]. The lines are a fit to the particle spectra with a hydrodynamically inspired model (blast wave). The fit describes all the particle spectra rather well which shows that these spectra can be characterized by the two parameters of the model: a single kinetic freeze-out temperature and a common transverse flow velocity. Figure 9c shows the combined pion, Kaon and proton p_t-spectra from the four RHIC experiments. Also at these energies, a common fit to all the spectra shows that the system seems to freeze-out with a temperature and with a transverse flow velocity similar to that observed at SPS energies.

2.1.8. Anisotropic flow

Because heavy-ions are not point-like, the size and shape of the collision region depends on the distance between the centers of the nuclei in the transverse plane (impact parameter **b**). The plane defined by the impact parameter

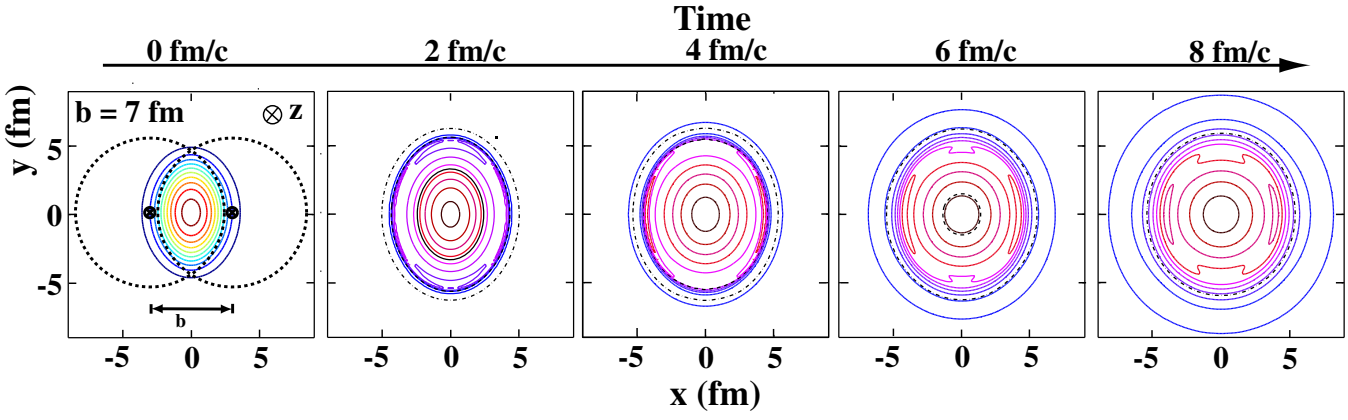

Figure 10: The created initial transverse energy density profile [45] and its time dependence in coordinate space for a non-central heavy-ion collision. The z-axis is along the colliding beams, the x-axis is defined by the impact parameter $\mathbf{b}$ (the vector connecting the centers of the colliding heavy-ions, perpendicular on the beam axis).

and the beam direction (z) is called the reaction plane. Figure 10 shows the initial spatial distribution of a non-central ($\mathbf{b} \neq 0$) heavy-ion collision in the transverse plane. The created medium in these non-central collisions has an azimuthal asymmetry in coordinate space which translates, due to multiple interactions, into an azimuthal asymmetry in momentum space. In this way, measurements of the azimuthal asymmetry yields information on the properties of the produced medium without making use of proton-proton or proton-nucleus reference data.

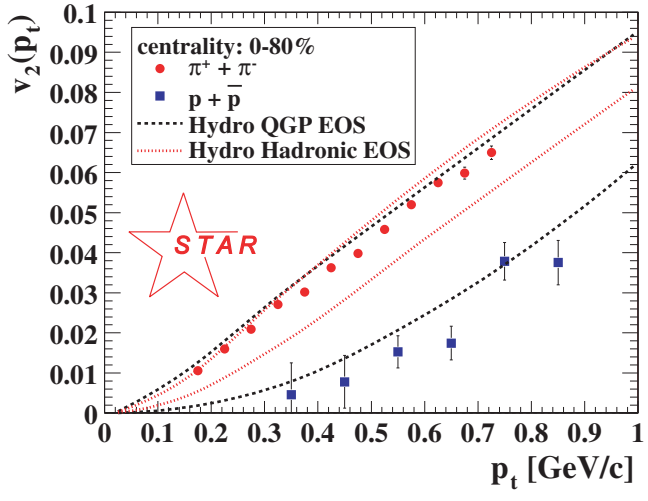

Figure 11: $v_2(p_t)$ for pions and protons at $\sqrt{s_{NN}} = 130$ [46]. The lines are hydrodynamical model calculations [47].

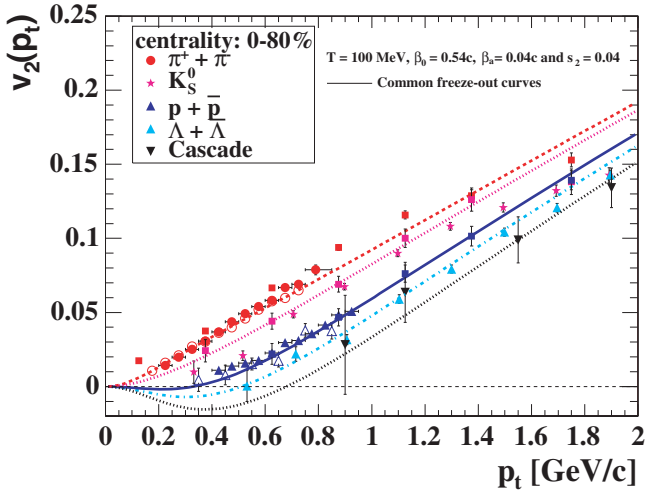

Figure 12: $v_2(p_t)$ for identified particles compared to a blast wave fit [46, 48–50].

The asymmetry can be described by [51]:

$$E\frac{\mathrm{d}^3N}{\mathrm{d}^3p} = \frac{1}{2\pi}\frac{\mathrm{d}^2N}{p_t \mathrm{d}p_t \mathrm{d}y}[1 + \sum_{n=1}^{\infty} 2v_n \cos(n\phi)]$$

where ϕ is the azimuthal angle with respect to the reaction plane and v_2 is the coefficient of the second harmonic, called elliptic flow. The magnitude of v_2 and its p_t dependence allow for the extraction of the kinetic freeze-out temperature and the transverse flow velocity as function of emission angle.

Figure 11 shows the measurement of v_2 versus p_t for pions and protons (plus antiprotons), compared to hydrodynamical models calculations using a QGP and a hadron gas equation of state [47]. It is evident from this figure that

v_2 depends on the particle mass and that the flow of the heavier particle (protons) is consistent with the assumption of a QGP EoS. In Fig. 12, RHIC data on $v_2(p_t)$ for various particles are compared to a hydrodynamically inspired fit [46, 48–50]. The agreement of the data with the fit shows that the $v_2(p_t)$ for all particles can be described in terms of a single temperature and one ϕ-dependent transverse flow velocity. The agreement with hydrodynamical calculations lends support to the underlying assumption that the system is partonic and thermalized at the early stage of the collision.

2.1.9. Jet quenching

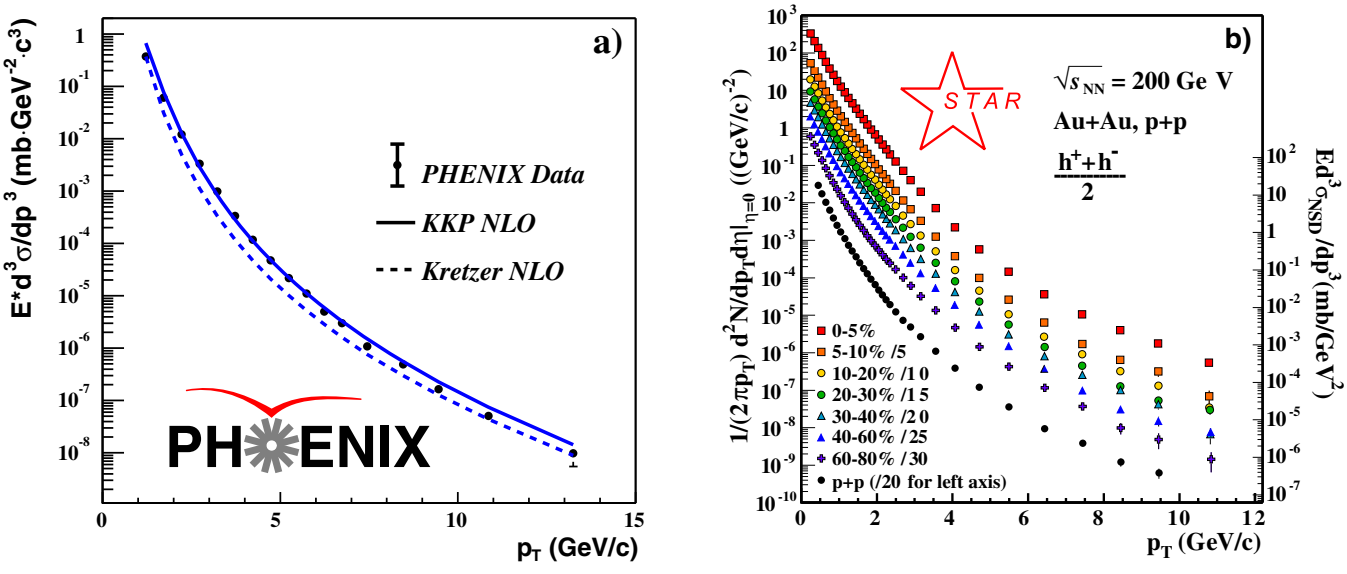

Figure 13: π_0 spectra in p-p [53] and charged hadrons in p-p and Au+Au [54–56].

At the highest RHIC energies (200 GeV), jets with transverse energies above 40 GeV are produced in abundance, providing a detailed probe of the created system. However the abundant soft particle production tends to obscure the characteristic jet structures. At sufficient high-p_t, jets can be identified by their leading particles because the contribution from the tails of the soft particle production become negligible. It is argued in [52] that a leading parton traversing a dense system loses energy by induced gluon radiation, giving rise to the so-called jet-quenching phenomenon. The amount of energy loss is in this picture directly related to the parton density (mainly gluons at RHIC) of the created system.

Figure 13a shows the π_0 spectrum as measured in p-p at $\sqrt{s_{\rm NN}}$ = 200 GeV by PHENIX. It is seen that this spectrum is well described by NLO perturbative QCD (see the curves in the figure). In Fig. 13b are shown the charged hadron spectra measured by STAR in Au-Au at $\sqrt{s_{\rm NN}}$ = 200 GeV together with the p-p reference spectra measured at the same energy.

The standard way to compare A-A collisions to the p-p baseline is via the so-called nuclear modification factor defined by

$$R_{\rm AA}(p_{\rm t}) = \frac{{\rm d}^2\sigma_{\rm AA}/{\rm d}y{\rm d}p_{\rm t}}{\langle N_{\rm binary}\rangle {\rm d}^2\sigma_{\rm pp}/{\rm d}y{\rm d}p_{\rm t}}.$$

Here ${\rm d}^2\sigma_{\rm pp}/{\rm d}y{\rm d}p_{\rm t}$ is the inclusive cross section measured in p-p collisions and $\langle N_{\rm binary}\rangle$ accounts for the geometrical scaling from p-p to nuclear collisions. In case that a Au+Au collision is an incoherent sum of p-p collisions, this ratio would be unity. Nuclear effects like energy loss and shadowing will reduce this ratio below unity while anti-shadowing and the so-called Cronin effect leads to a value above unity. Figure 14a and b show $R_{\rm AA}$ for charged particles and

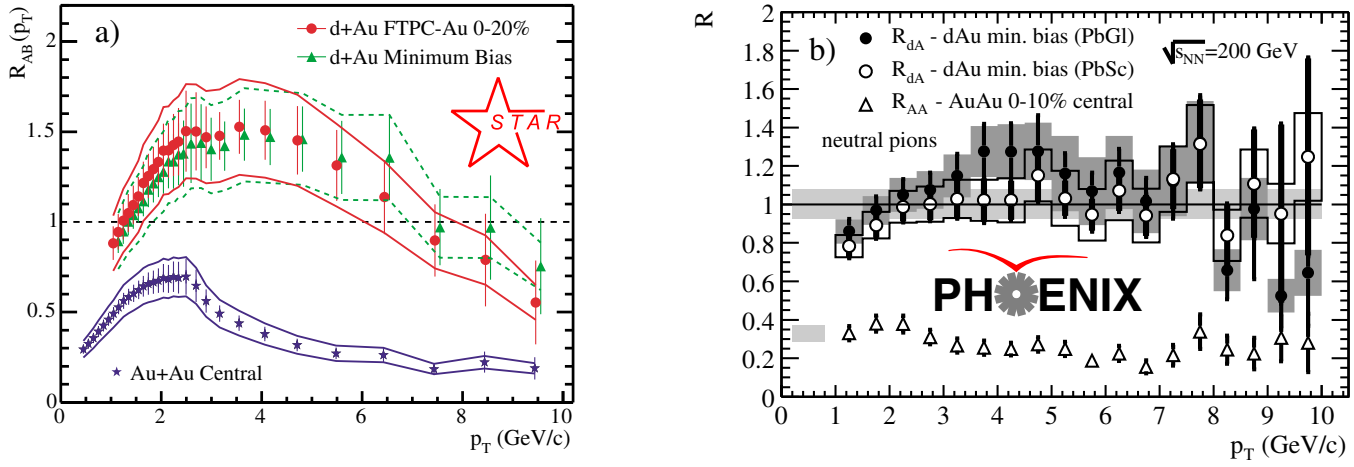

Figure 14: d+AU and Au+Au measurements from a) STAR [54–56] and b) PHENIX [57–61].

π_0's in central Au+Au collisions at mid-rapidity. The ratio is well below unity for all p_t with the suppression reaching a factor of 5 at high p_t. At intermediate p_t the suppression of charged particles and π_0 differ by a factor of two.

To discriminate between final and initial state effects, d-Au collisions were measured at RHIC. If the suppression is due to initial state effects it should also be observed in the d-Au system. Figure 14a and b also show the d-Au nuclear modification factor for charged particles and π_0, respectively. It is clear that in d+Au interactions no suppression is observed but, instead, a small enhancement consistent with the Cronin effect. Therefore the observed suppression in Au-Au is due to final state effects and indicate, in the jet quenching picture, that the density of the created medium is a factor 30 higher than the density of cold nuclear matter.

To study the effect of jet quenching in greater detail, azimuthal correlations between particles can be used. The azimuthal correlations of two high-p_t particles from jets are expected to show a narrow near-side correlation and a broader away-side correlation. However, in the case of strong jet quenching the away-side jet would be suppressed by energy loss in the traversed medium. The azimuthal correlations of high-p_t particles (trigger particle $4 < p_t < 6$ GeV/c, associated particle 2 GeV/$c < p_t < p_t^{trig}$) measured in p-p collisions at RHIC by STAR are shown as the histogram in Figure 15b. The near-side and away-side peaks are clearly visible. The correlation function observed in central Au+Au collisions (stars in Fig. 15b) shows a similar near side peak while the away-side peak has disappeared. To investigate if this is due to initial state effects, the same analysis was done for d+Au collisions. In Fig. 15a the near and away-side peaks are shown for minimum bias and central d+Au collisions compared to p-p. The away-side correlation in d+Au is clearly observed even for the most central collisions. Comparing the results obtained in p-p, d+Au and Au+Au, Fig. 15b, shows that the suppression only occurs in Au+Au collisions and therefore is a final state effect as expected from partonic energy loss mechanisms.

3. HEAVY IONS AT THE LHC

The LHC at CERN will provide colliding Pb ions with an energy of $\sqrt{s_{NN}} = 5.5$ TeV. This exceeds the maximum energy of 200 GeV available at RHIC by a factor 30 ad will open up a new physics domain. Qualitative new features of the heavy-ion collisions at the LHC include:

- Particle production is determined by high-density saturated parton distributions.

  The LHC heavy-ion program accesses a novel range of low Bjorken-x values (see Fig. 16), where strong nuclear shadowing is expected. The initial density of gluons is expected to be close to saturation of the available phase space. These very high initial densities allow to describe important aspects of the subsequent time evolution

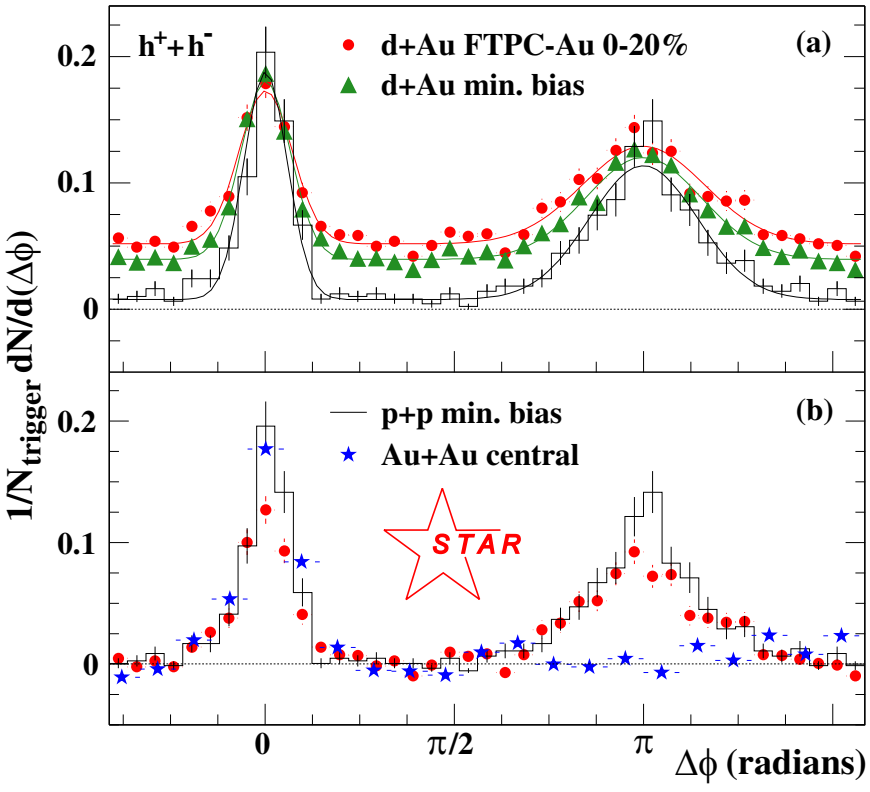

Figure 15: a,b) Back to back correlations [62].

in terms of classical chromodynamics [63, 64]. The ALICE detector will probe a continuous range of x as low as $\sim 10^{-5}$.

- Hard processes become abundant.

  The abundance of hard processes at the LHC will allow for precision test of perturbative QCD. In addition, the large jet rates at the LHC permit detailed measurements of jet quenching to study the early stages of the collision.

- Access to weakly interacting hard probes.

  Direct photons as well as Z^0 and $W^{\pm}$ bosons produced in hard processes will provide information about nuclear parton distributions at high Q^2. Jet tagging with such probes yields a calibrated energy scale for jet quenching studies.

- Fireball expansion is dominated by parton dynamics.

  Due to the expected longer lifetime of the QGP, the parton dynamics will dominate over the hadronic contribution to the fireball expansion and the collective features of the event.

Of course, the large increase in center of mass energy provided by the LHC will offer unique opportunities for new and unexpected discoveries.

It is expected that the LHC can deliver luminosities of 10^{27} cm^2 s^{-1} for Pb-Pb collisions, which results in a minimum-bias interaction rate of 8 kHz. Lighter ions can be delivered with higher luminosities of up to 10^{29} cm^2 s^{-1}, corresponding to an interaction rate of several 100 kHz. The machine can deliver p-p luminosities up to 10^{31} cm^2 s^{-1} but because of detector limitations this luminosity is restricted to 10^{30} cm^2 s^{-1} for ALICE.

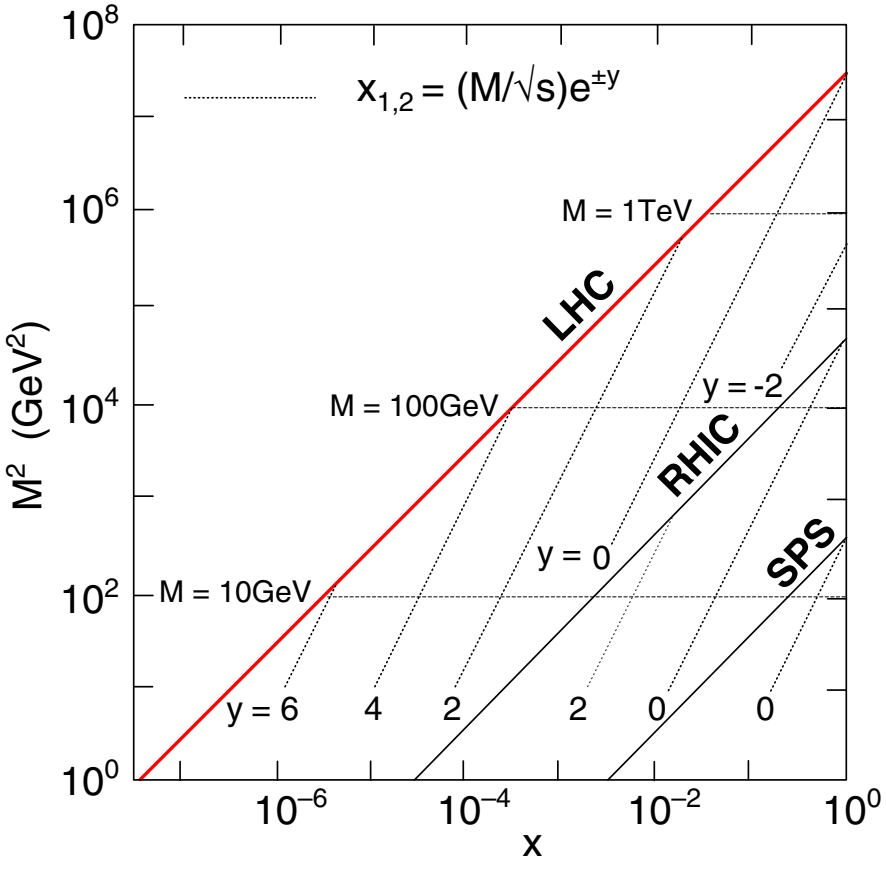

Figure 16: The range of Bjorken $x_{1,2}$ and M^2, relevant for particle production in nucleus-nucleus collisions at the top SPS ($\sqrt{s_{NN}} = 17.2$ GeV), RHIC ($\sqrt{s_{NN}} = 200$ GeV) and LHC ($\sqrt{s_{NN}} = 5.5$ TeV) energies.

4. THE ALICE DETECTOR

To study heavy-ion collisions at the LHC the ALICE collaboration has designed a general purpose detector optimized to measure a large variarity of observables. The apparatus will detect and identify hadrons, leptons and photons over a wide range of momenta. The requirement to study the various probes of interest in a very high multiplicity environment, which may be as large as 8 000 charged particles per unit of rapidity in central Pb-Pb collisions, imposes severe demands on the tracking of charged particles.

The ALICE detector (see Fig. 17) consists of a central part, which measures hadrons, electrons and photons, and a forward spectrometer to measure muons. The central barrel is placed inside the L3 magnet which provides a solenoidal field up to 0.5 T. The central tracking detector covers a range of $|\eta| < 0.9$ and a full range in azimuth. It consists of an Inner Tracking System (ITS), a Time-Projection Chamber (TPC), a single arm electromagnetic calorimeter (PHOS), a Time-of-Flight detector (TOF), a Transition Radiation Detector (TRD) and a single-arm ring imaging Cherenkov (HMPID). The muon spectrometer covers a range of $-4.0 < \eta < -2.5$ and consists of an arrangement of absorbers, a large dipole magnet and fourteen planes of tracking and triggering chambers. Several smaller detectors (ZDC, PMD, FMD, T0, V0) are located at forward angles and used for global event characterization and triggering (not shown in the figure). The ACORDE array of scintillators, on top of the L3 magnet, will be used to trigger on cosmic rays.

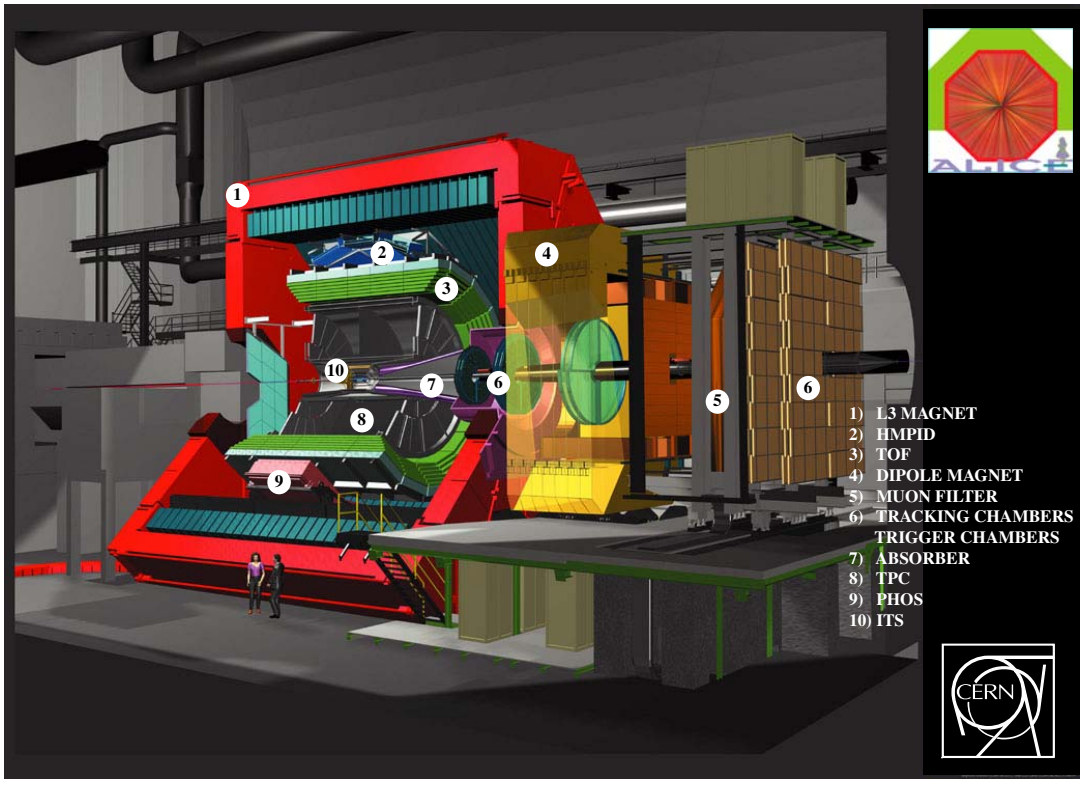

Figure 17: The ALICE detector layout

4.1. Detector performance

Figure 18 shows the particle tracks originating from a single heavy-ion collision in the ALICE detector. In ALICE the two innermost ITS silicon pixel layers are used to find the primary collision vertex. In central, high multiplicity, Pb-Pb collisions the vertex is reconstructed with a precision of about 5 μm in the beam direction and about 25 μm in the transverse plane. For p-p collisions, with much lower multiplicities, the vertex resolution is worse by about a factor of 10.

In ALICE, tracks are initially found in the TPC. Provided that there is a sufficient number of hits in the TPC, the track finding efficiency is almost 100% for $p_{\rm t}$ above 0.2 GeV/c. With a magnetic field of 0.5 T, the TPC momentum resolution is about 0.7% at $p_{\rm t}$ = 1 GeV/c. It has been verified that these performances can be reached at even the highest expected multiplicities of 8 000 charged particles per unit of rapidity.

The tracks reconstructed in the TPC are propagated inwards to the ITS. With the ITS, the impact parameter of 1 GeV/c tracks in central Pb-Pb collisions can be measured with an resolution of 50 μm. Due to the lower multiplicity, this resolution is about 100 μm in p-p collisions. The ITS is not only important for precision reconstruction of the primary and secondary vertices but also substantially improves the momentum resolution of the TPC at high $p_{\rm t}$. Combined tracking in the TRD, TPC and ITS results in a momentum resolution of about 3.5% for $p_{\rm t}$ = 100 GeV/c and a magnetic field of 0.5 T.

The identification of charged hadrons is done by combining the PID information provided by the ITS, TPC, TRD, TOF, and HMPID detectors. With the particle abundances expected for 5.5 TeV Pb-Pb collisions, the efficiency of the PID algorithm is found to be above 95% for pions up to about 6 GeV/c, above 60% for Kaons up to 3 GeV/c, and above 70% for protons up to 5 GeV/c. The overall effective PID efficiency is limited by particle decays and absorption in the detector material. When integrated over momentum the efficiency is about 50% for pions and protons, and 40% for Kaons. Electrons with momentum above 1 GeV/c are identified by the TRD with an efficiency of more than 90% and with the pion rejection factor of about 100.

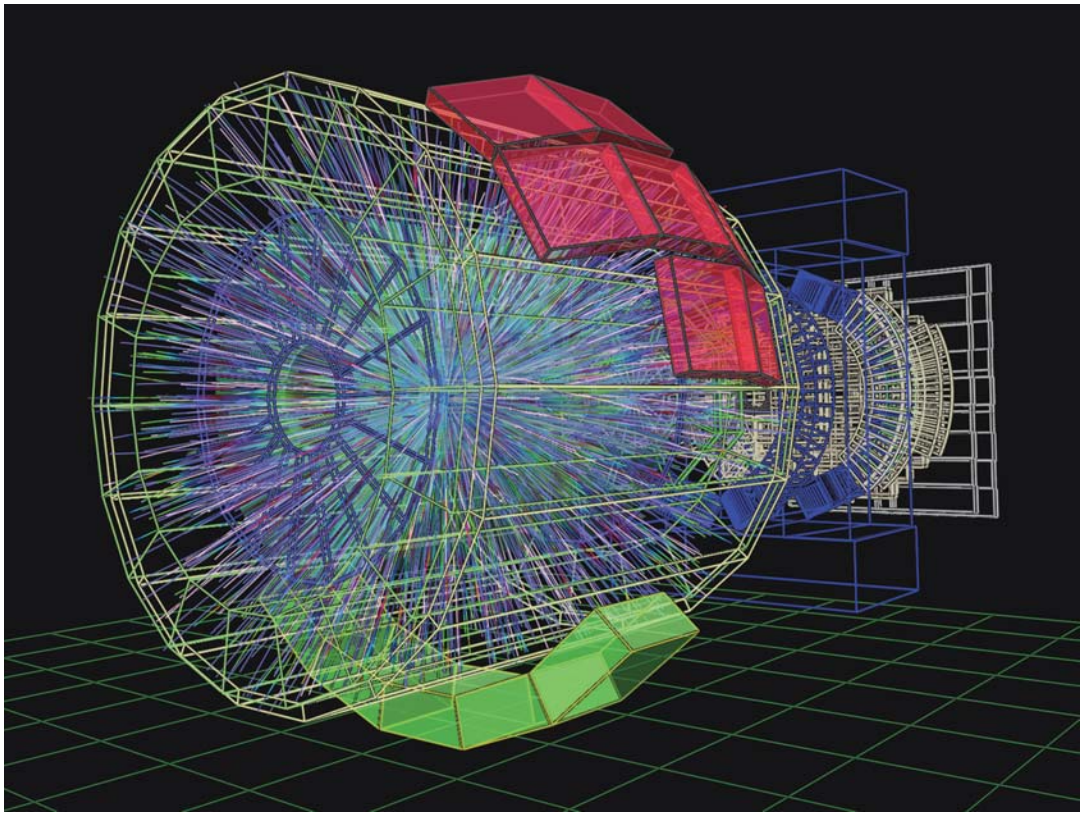

Figure 18: Particle tracks from a single simulated heavy-ion collision in ALICE

The track finding efficiency in the muon arm is found to be about 95%. The invariant mass resolution is better than 100 MeV/c^2 which is sufficient to resolve the different quarkonia states.

The PHOS spectrometer detects and identifies photons with high energy and position resolution. In the momentum range below ∼20 GeV/c the direct photon spectrum is obtained from subtraction of the decay photon contribution to the overall identified photon spectrum. These decay contributions are estimated from the measured spectra of light neutral mesons. In the high-momentum range direct photons are identified on an event by event basis by the shower shape and by using isolation-cut discrimination techniques. The identification efficiency for photons with energies $0.5 < E_\gamma < 40$ GeV is above 50% in Pb-Pb collisions and above 90% in p-p interactions.

The Photon Multiplicity Detector (PMD) counts photons in the forward rapidity region $2.3 < \eta < 3.5$. The photon reconstruction efficiency is a function of pseudorapidity with a maximum of about 70% at $\eta = 2.6$. The purity of the PMD photon sample is above 60% in the whole covered range of pseudorapidities.

4.2. Physics performance

In ALICE, the collision geometry can be estimated from the energy deposited in the ZDCs or from the multiplicity measured by the FMD and the two innermost layers of the ITS over 8 units in pseudorapidity. The excellent PID capabilities, momentum resolution and complete azimuthal coverage of the central detectors allow comprehensive measurements of particle ratios, momentum spectra, particle correlations, anisotropic flow and event-by-event fluctuations. These observables do not require large amounts of data and will either quickly confirm our current understanding of high density QCD or provide fundamental new insights.

The LHC will be the first machine where heavy quarks are produced abundantly in heavy-ion collisions. Due to the excellent impact parameter resolution and particle identification capabilities, ALICE is well suited to study charm and beauty. From detailed simulation studies of the benchmark channel $D^0 \rightarrow K^-\pi^+$ it is found that in one

LHC year at nominal luminosity, we cover the transverse momentum range $1 < p_{\rm t} < 18$ GeV/c in the central barrel acceptance of $|\eta| < 0.9$. Beauty production can be measured from semi-leptonic decays in the range of $2 < p_{\rm t} < 30$ GeV/c. Single muons and opposite-sign dimuon pairs detected in the muon spectrometer allow for measurements of open-beauty production with high statistics in the pseudorapidity region $-4 < \eta < -2.5$. The measurement of heavy flavor production down to very low transverse momenta is sensitive to the collective motion of heavy quarks in the medium and will provide strong constraints on the thermalization of light quarks. At higher momenta, on the other hand, the measurement of heavy flavor production will provide detailed information on the energy loss mechanism.

In addition to open charm and open beauty, the complete spectrum of heavy quarkonia states (J/Ψ, Ψ', Υ, Υ' and Υ") is accessible at the LHC. In ALICE quarkonia are detected at mid-rapidity ($-0.9 < \eta < 0.9$) in the dielectron channel, and at ($-4.0 < \eta < -2.5$) in the dimuon channel, which will allow for detailed studies of suppression effects due to deconfinement.

The jet rates in central Pb-Pb collisions at the LHC in the ALICE acceptance are sufficient to map out the energy dependence of jet fragmentation over a wide kinematic range up to $E_{\rm t} \simeq 200$ GeV. Jet reconstruction in nuclear collisions has to cope with the large background from the underlying event, therefore, jet reconstruction has to be limited to a small cone of fixed radius in azimuth and pseudorapidity ranging between 0.3 – 0.5. In addition, a transverse momentum cut in the range 1–2 GeV/c has to be applied to reduce the background. As a consequence, even for perfect calorimetry, the transverse energy resolution is limited to $\simeq 20\%$. In its present design, ALICE can measure only the charged particles within the jets, limiting the jet-energy resolution to 40 – 50%. Nevertheless, at high $E_{\rm t}$, charged jet reconstruction is shown to be much superior for studying high-$p_{\rm t}$ parton fragmentation compared to using leading particles only, because the bias in the fragmentation function is significantly reduced. The proposed electromagnetic calorimeter for ALICE will improve the jet-energy resolution, which further reduces the bias on the jet fragmentation. In addition, it will add a trigger which is needed to increase the statistics at high $E_{\rm t}$. Another very promising approach to study jet fragmentation is using prompt photons to tag charged jets emitted in the opposite direction. Prompt photons allow to study the hard interaction without any final state modifications and with this tag the in-medium modification of the fragmentation function will be measured with an accuracy of the order of a few per cent. The combined tracking capabilities of the ALICE detector combined with electromagnetic calorimetry represent an ideal tool for jet structure modifications at the LHC.

5. SUMMARY

The construction of the LHC machine and the ALICE detector are nearing completion. In 2007 we are expecting the first p-p collisions (at lower energies) and in 2008 p-p collisions at design energy as well as the first heavy-ion collisions. The ALICE detector at the LHC will allow us to explore new aspects of the structure of strongly interacting nuclear matter and detailed studies of the QGP. Much of the material presented here has been taken from the ALICE Physics Performance Reports [65, 66]. These PPR's, combined more than a thousand pages, provide a much more detailed description of both the ALICE detector and its physics program.

Acknowledgments

The author would like to thank M. Botje for his help with preparing this document. This work is supported by NWO and FOM.

References

[1] J.L. Nagle. This proceedings.

[2] *Connecting Quarks with the Cosmos: Eleven Science Questions for the New Century.* The National Academies Press, 2003.
[3] DOE/NSF. Quantum Universe, 2004.
[4] Peter W. Higgs. Broken symmetries, massless particles and gauge fields. *Phys. Lett.*, 12:132–133, 1964.
[5] Peter W. Higgs. Broken symmetries and the masses of gauge bosons. *Phys. Rev. Lett.*, 13:508–509, 1964.
[6] F. Englert and R. Brout. Broken symmetry and the mass of gauge vector mesons. *Phys. Rev. Lett.*, 13:321–322, 1964.
[7] Yoichiro Nambu and G. Jona-Lasinio. Dynamical model of elementary particles based on an analogy with superconductivity. i. *Phys. Rev.*, 122:345–358, 1961.
[8] D. J. Gross and Frank Wilczek. Asymptotically free gauge theories. 1. *Phys. Rev.*, D8:3633–3652, 1973.
[9] H. David Politzer. Reliable perturbative results for strong interactions? *Phys. Rev. Lett.*, 30:1346–1349, 1973.
[10] F. Karsch and E. Laermann. Thermodynamics and in-medium hadron properties from lattice QCD. In R.C. Hwa, editor, *Quark gluon plasma*, pages 1–59. 2003.
[11] G. F. Chapline, M. H. Johnson, E. Teller, and M. S. Weiss. Highly excited nuclear matter. *Phys. Rev.*, D8:4302–4308, 1973.
[12] T. D. Lee and G. C. Wick. Vacuum stability and vacuum excitation in a spin 0 field theory. *Phys. Rev.*, D9:2291, 1974.
[13] T. D. Lee. Feynman rules of QCD inside a hadron. *Phys. Rev.*, D19:1802, 1979.
[14] John C. Collins and M. J. Perry. Superdense matter: Neutrons or asymptotically free quarks? *Phys. Rev. Lett.*, 34:1353, 1975.
[15] Edward V. Shuryak. Quantum chromodynamics and the theory of superdense matter. *Phys. Rept.*, 61:71–158, 1980.
[16] Robert D. Pisarski and Frank Wilczek. Remarks on the chiral phase transition in chromodynamics. *Phys. Rev.*, D29:338–341, 1984.
[17] K. Adcox et al. Measurement of the mid-rapidity transverse energy distribution from $\sqrt{s_{\rm NN}} = 130$ GeV Au + Au collisions at RHIC. *Phys. Rev. Lett.*, 87:052301, 2001.
[18] J. D. Bjorken. Highly relativistic nucleus-nucleus collisions: The central rapidity region. *Phys. Rev.*, D27:140–151, 1983.
[19] B. B. Back et al. The significance of the fragmentation region in ultrarelativistic heavy ion collisions. *Phys. Rev. Lett.*, 91:052303, 2003.
[20] T. Matsui and H. Satz. J/Ψ suppression by quark - gluon plasma formation. *Phys. Lett.*, B178:416, 1986.
[21] M. C. Abreu et al. Evidence for deconfinement of quarks and gluons from the J/Ψ suppression pattern measured in Pb+Pb collisions at the CERN-SPS. *Phys. Lett.*, B477:28–36, 2000.
[22] A. Adare. J/Ψ production vs centrality, transverse momentum, and rapidity in Au + Au collisions at $\sqrt{s_{\rm NN}} =$ 200 GeV. 2006.
[23] S. S. Adler et al. J/Ψ production and nuclear effects for d + Au and p + p collisions at $\sqrt{s_{\rm NN}} = 200$ GeV. *Phys. Rev. Lett.*, 96:012304, 2006.
[24] R. L. Thews, M. Schroedter and J. Rafelski. Enhanced J/psi production in deconfined quark matter. *Phys. Rev.*, **C63**:054905, 2001.
[25] Johann Rafelski and Berndt Muller. Strangeness production in the quark - gluon plasma. *Phys. Rev. Lett.*, 48:1066, 1982.
[26] Johann Rafelski. Formation and observables of the quark - gluon plasma. *Phys. Rept.*, 88:331, 1982.
[27] P. Koch, B. Muller, and J. Rafelski. Strangeness in relativistic heavy ion collisions. *Phys. Rept.*, 142:167–262, 1986.
[28] Johann Rafelski. Strange anti-baryons from quark - gluon plasma. *Phys. Lett.*, B262:333–340, 1991.
[29] E. Andersen et al. Strangeness enhancement at mid-rapidity in Pb + Pb collisions at 158 A GeV/c. *Phys. Lett.*, B449:401–406, 1999.
[30] C. Alt et al. System-size dependence of strangeness production in nucleus nucleus collisions at $\sqrt{s_{\rm NN}} = 17.3$ GeV.

Phys. Rev. Lett., 94:052301, 2005.

[31] Salah Hamieh, Krzysztof Redlich, and Ahmed Tounsi. Canonical description of strangeness enhancement from p-A to Pb-Pb collisions. *Phys. Lett.*, B486:61–66, 2000.

[32] G. E. Brown and Mannque Rho. Scaling effective lagrangians in a dense medium. *Phys. Rev. Lett.*, 66:2720–2723, 1991.

[33] G. E. Brown and Mannque Rho. Chiral restoration in hot and/or dense matter. *Phys. Rept.*, 269:333–380, 1996.

[34] R. Rapp and J. Wambach. Chiral symmetry restoration and dileptons in relativistic heavy-ion collisions. *Adv. Nucl. Phys.*, 25:1, 2000.

[35] R. Arnaldi et al. First measurement of the rho spectral function in high- energy nuclear collisions. *Phys. Rev. Lett.*, 96:162302, 2006.

[36] P. Braun-Munzinger, D. Magestro, K. Redlich, and J. Stachel. Hadron production in Au + Au collisions at RHIC. *Phys. Lett.*, B518:41–46, 2001.

[37] Francesco Becattini. A thermodynamical approach to hadron production in e+ e- collisions. *Z. Phys.*, C69:485–492, 1996.

[38] Ulrich Heinz and Gregory Kestin. Universal chemical freeze-out as a phase transition signature. nucl-th/0612105, 2006.

[39] M. van Leeuwen. Energy dependence of particle production in nucleus nucleus collisions at the CERN SPS. nucl-ex/0306004, 2003.

[40] Thomas S. Ullrich. Characteristics of charged particle production in relativistic heavy-ion collisions. *Heavy Ion Phys.*, 21:143–150, 2004.

[41] I. G. Bearden. From y=0 to y=3: Recent results from BRAHMS. *Nucl. Phys.*, A715:171–179, 2003.

[42] Barbara Wosiek et al. Identified particles in Au + Au collisions at $\sqrt{s_{\rm NN}} = 200$ GeV. *Nucl. Phys.*, A715:510–513, 2003.

[43] John Adams et al. Identified particle distributions in p + p and Au + Au collisions at $\sqrt{s_{\rm NN}} = 200$ GeV. *Phys. Rev. Lett.*, 92:112301, 2004.

[44] S. S. Adler et al. Identified charged particle spectra and yields in Au + Au collisions at $\sqrt{s_{\rm NN}} = 200$ GeV. *Phys. Rev.*, C69:034909, 2004.

[45] Peter F. Kolb and Ulrich Heinz. Hydrodynamic description of ultrarelativistic heavy-ion collisions. In R.C. Hwa, editor, *Quark gluon plasma*, pages 634–714. 2003.

[46] C. Adler et al. Identified particle elliptic flow in Au + Au collisions at $\sqrt{s_{\rm NN}} = 130$ GeV. *Phys. Rev. Lett.*, 87:182301, 2001.

[47] P. Huovinen, P. F. Kolb, and Ulrich W. Heinz. Is there elliptic flow without transverse flow? *Nucl. Phys.*, A698:475–478, 2002.

[48] J. Adams et al. Particle dependence of azimuthal anisotropy and nuclear modification of particle production at moderate $p_{\rm t}$ in Au + Au collisions at $\sqrt{s_{\rm NN}} = 200$ GeV. *Phys. Rev. Lett.*, 92:052302, 2004.

[49] Raimond Snellings. Elliptic flow measurements from STAR. *Heavy Ion Phys.*, 21:237–242, 2004.

[50] ShinIchi Esumi. Identified charged particle azimuthal anisotropy in PHENIX at RHIC. *Nucl. Phys.*, A715:599–602, 2003.

[51] S. Voloshin and Y. Zhang. Flow study in relativistic nuclear collisions by fourier expansion of azimuthal particle distributions. *Z. Phys.*, C70:665–672, 1996.

[52] Miklos Gyulassy and Michael Plumer. Jet quenching in dense matter. *Phys. Lett.*, B243:432–438, 1990.

[53] S. S. Adler et al. Suppressed π_0 production at large transverse momentum in central Au + Au collisions at $\sqrt{s_{\rm NN}}$ = 200 GeV. *Phys. Rev. Lett.*, 91:072301, 2003.

[54] C. Adler et al. Centrality dependence of high $p_{\rm t}$ hadron suppression in Au + Au collisions at $\sqrt{s_{\rm NN}} = 130$ GeV. *Phys. Rev. Lett.*, 89:202301, 2002.

[55] John Adams et al. Transverse momentum and collision energy dependence of high $p_{\rm t}$ hadron suppression in Au + Au collisions at ultrarelativistic energies. *Phys. Rev. Lett.*, 91:172302, 2003.

[56] John Adams et al. Evidence from d + Au measurements for final-state suppression of high $p_{\rm t}$ hadrons in Au +

Au collisions at RHIC. *Phys. Rev. Lett.*, 91:072304, 2003.

[57] K. Adcox et al. Suppression of hadrons with large transverse momentum in central Au + Au collisions at $\sqrt{s_{\rm NN}}$ = 130 GeV. *Phys. Rev. Lett.*, 88:022301, 2002.

[58] K. Adcox et al. Centrality dependence of the high $p_{\rm t}$ charged hadron suppression in Au + Au collisions at $\sqrt{s_{\rm NN}}$ = 130 GeV. *Phys. Lett.*, B561:82–92, 2003.

[59] S. S. Adler et al. Absence of suppression in particle production at large transverse momentum in $\sqrt{s_{\rm NN}}$ = 200 GeV d + Au collisions. *Phys. Rev. Lett.*, 91:072303, 2003.

[60] S. S. Adler et al. Scaling properties of proton and anti-proton production in $\sqrt{s_{\rm NN}}$ = 200 GeV Au + Au collisions. *Phys. Rev. Lett.*, 91:172301, 2003.

[61] S. S. Adler et al. High-$p_{\rm t}$ charged hadron suppression in Au + Au collisions at $\sqrt{s_{\rm NN}}$ = 200 GeV. *Phys. Rev.*, C69:034910, 2004.

[62] C. Adler et al. Disappearance of back-to-back high $p_{\rm t}$ hadron correlations in central Au + Au collisions at $\sqrt{s_{\rm NN}}$ = 200 GeV. *Phys. Rev. Lett.*, 90:082302, 2003.

[63] Larry D. McLerran and Raju Venugopalan. Computing quark and gluon distribution functions for very large nuclei. *Phys. Rev.*, D49:2233–2241, 1994.

[64] Larry D. McLerran and Raju Venugopalan. Gluon distribution functions for very large nuclei at small transverse momentum. *Phys. Rev.*, D49:3352–3355, 1994.

[65] Carminati, F. (ed.) et al. Alice: Physics performance report, volume I. *J. Phys.*, G30:1517–1763, 2004.

[66] B. Alessandro et al. Alice: Physics performance report, volume II. *J. Phys.*, G32:1295–2040, 2006.